International Journal of Refrigeration 150 (2023) 253–264

Contents lists available at ScienceDirect

International Journal of Refrigeration

journal homepage: www.elsevier.com/locate/ijrefrig

Vacuum swing adsorption for R-32 recovery from R-410A refrigerant blend

Cycle à adsorption oscillatoire sous vide pour la récupération du R-32 à partir d'un mélange de frigorigènes R-410A

Rui P.P.L. Ribeiro *, Julio E. Sosa, João M.M. Araújo, Ana B. Pereiro, José P.B. Mota

LAQV-REQUIMTE, Department of Chemistry, NOVA School of Science and Technology, NOVA University of Lisbon, 2829-516, Caparica, Portugal

ARTICLE INFO

Keywords:
Greenhouse gases
Fluorinated gases
Recycling
VSA
Activated carbon
Mots clés:
Gaz à effet de serre
Gaz fluorés
Recyclage
Cycle à adsorption oscillatoire sous vide
Charbon actif

ABSTRACT

The recovery of high purity fluorinated gases from refrigerant blends is vital to promote a circular economy in the field of refrigeration and air conditioning. In this work, we evaluate the performance of a four-step Vacuum Swing Adsorption (VSA) process using activated carbon for the recovery of R-32 (difluoromethane) from a R-410A refrigerant blend: a binary mixture of R-125 (pentafluoroethane) and R-32 ($y_{R-32} = 0.7$; $y_{R-125} = 0.3$). Breakthrough curves were performed using dilute and bulk feed concentrations to determine mass and heat transfer parameters, which were then employed in simulations of fixed-bed adsorber dynamics. The mathematical model employed successfully predicts the experimental results of a four-step VSA cycle (feed, blowdown, purge, pressurization). The VSA performance was evaluated using process simulation. For a cycle time of 800 s (each step taking 200 s) and feed and regeneration pressures of 1.01 and 0.01 bar, respectively, R-32 is obtained with 97.0 mol-% purity and 30.9% recovery, with process productivity of 4.06 mol h^{-1} per kilogram of adsorbent, and energy consumption of 123.2 kJ/mol. Our results demonstrate the feasibility of using VSA processes for the recovery of R-32 from the near-azeotropic R-410A refrigerant blend.

1. Introduction

Fluorinated gases (F-gases), including hydrofluorocarbons (HFCs), are compounds with numerous industrial applications, of which refrigeration and air conditioning systems are two of the most significant (European Comission, 2022). Among other advantages, F-gases have low toxicity and flammability, and do not affect the ozone layer (U.S. EPA, 2022). For this reason, after the Montreal protocol, F-gases began to be massively employed in the replacement of ozone-depleting species such as chlorofluorocarbons (CFCs) and hydrochlorofluorocarbons (HCFCs). Although this had a positive impact in the ozone layer, the high global warming potential (GWP) of F-gases has worsened other climate-related problems. Their GWP can be 25,000 higher than carbon dioxide and they persist in the atmosphere for a long time (up to 50,000 years) (U.S.EPA, 2022). Therefore, legislation has been implemented to regulate their emissions. The Kigali international agreement (2016) and, even to a greater extent, the EU regulation (EU No 517/2014), have established international regulation to decrease the emission of F-gases to the atmosphere (Heath, 2017; Mota-Babiloni et al., 2017).

In recent years, the refrigeration and air conditioning market has been based in the so-called third-generation refrigerants. R-410A is one of the most used refrigerants, consisting in a binary mixture of HFCs R-32 (difluoromethane) and R-125 (pentafluoroethane) composed by 70 mol-% R-32 and 30 mol-% R-125 (50 wt-% R-32 / 50 wt-% R-125). This refrigerant blend, as well as other similar ones, has a very high GWP (2088), reason why its utilization is being phased out (Mota-Babiloni et al., 2017). Alternatives with lower GWP include a fourth-generation refrigerants, such as hydrofluoroolefins (HFO) blended with small proportions of previously used HFCs. R-444A, R-447A, and R-448A are examples of next-generation refrigerants which include R-32 and/or R-125 in blends also containing HFOs (Mota-Babiloni et al., 2015). This demonstrates the importance of recovering and recycling currently used F-gases, not only to avoid their emission to the atmosphere but also to reuse them in lower GWP refrigerants. This approach promotes a circular economy. Despite the importance of this application, there is currently no commercial technology to recover pure streams of F-gases from used refrigerant mixtures. This is a field in which R&D efforts are especially needed to develop efficient and environmentally friendly processes. Several refrigerant blends have azeotropic or near-azeotropic

* Corresponding author.
E-mail address: rpp.ribeiro@fct.unl.pt (R.P.P.L. Ribeiro).

https://doi.org/10.1016/j.ijrefrig.2023.01.020
Received 13 October 2022; Received in revised form 22 January 2023; Accepted 22 January 2023
Available online 28 January 2023
0140-7007/© 2023 The Author(s). Published by Elsevier B.V. This is an open access article under the CC BY-NC-ND license (http://creativecommons.org/licenses/by-nc-nd/4.0/).

Nomenclature

Acronyms

AC	activated carbon
BET	Brunauer–Emmett–Teller
CFC	chlorofluorocarbon
CFDM	centred finite differences method
CSS	cyclic steady state
F-gases	fluorinated gases
GWP	global warming potential
HFC	hydrofluorocarbon
HCFC	hydrochlorofluorocarbon
HFO	hydrofluoroolefin
IL	ionic liquid
LDF	linear driving force
MOF	metal-organic framework
VSA	vacuum swing adsorption

Roman symbols

A_{BET}	BET surface area ($m^2\ g^{-1}$)
A	cross-sectional area (m^2)
b	affinity constant (bar^{-1})
$\widetilde{C}$	specific heat ($J\ kg^{-1}\ K^{-1}$)
C	gas phase concentration ($mol\ m^{-3}$)
d	diameter (m)
D_z	axial dispersion coefficient ($m^2\ s^{-1}$)
E_a	activation energy ($J\ mol^{-1}$)
F	molar flowrate ($mol\ s^{-1}$)
h_{cw}	heat transfer coefficient between adsorption bed and column wall ($W\ m^{-2}\ K^{-1}$)
k_{LDF}	LDF coefficient (s^{-1})
L	bed length (m)
P	pressure (bar)
Q	flowrate (slpm)
$\overline{q}$	adsorbed-phase concentration ($mol\ kg^{-1}$)
q^*	adsorbed-phase concentration in the equilibrium state ($mol\ kg^{-1}$)
q^∞	saturation capacity ($mol\ kg^{-1}$)
r	radius (m)
R_g	ideal gas constant ($J\ K^{-1}\ mol^{-1}$)
t	time (s)
T	temperature (K)
T_∞	external environment temperature (K)
U	overall heat transfer coefficient ($W\ m^{-2}\ K^{-1}$)
u	superficial velocity ($m\ s^{-1}$)
V	volume (m^3)
V_μ	specific pore volume ($m^3\ kg^{-1}$)
v	interstitial velocity ($m\ s^{-1}$)
y	molar fraction (-)
z	axial position (m)

Greek Symbols

α_w	ratio of the internal surface area to the column wall volume (m^{-1})
α_{wl}	ratio of the logarithmic mean surface area of the column shell to the volume of the column wall (m^{-1})
γ	ratio between the constant pressure and constant volume specific heats (-)
ΔH	heat of adsorption ($J\ mol^{-1}$)
ε	porosity (-)
η	mechanical efficiency of the vacuum pump (-)
λ	thermal conductivity ($W\ m^{-1}\ K^{-1}$)
μ	viscosity (Pa s)
ρ	density ($kg\ m^{-3}$)

Subscripts and Superscripts

b	bulk
c	column (fixed-bed)
g	gas
i	component *i*
in	inlet
k	adsorption site *k*
out	outlet
p	particle
s	solid adsorbent
t	total
w	column wall
0	infinite temperature

behavior, which limits their separation through conventional approaches such as distillation. Therefore, several studies regarding processes based on the use of membranes and/or ionic liquids (ILs) have recently appeared in the literature. The molecular-based soft-SAFT equation of state was employed to evaluate the potential of ILs containing different fluorinated anions as solvents in R-32/R-125 separation from R-410A refrigerant blend. The authors proposed an extractive distillation unit using a selected IL – [C_2mim][Tf_2N] (Asensio-Delgado et al., 2020). Pardo et al. reported for the first time the use of IL–polymeric membranes for the same separation. Highly stable membranes containing 40 wt-% [C_2mim][SCN] or [C_2mim][BF_4] showed a significant improvement in R-32 permeability and R-32/R-125 selectivity when compared with neat Pebax®1657 membranes (Pardo et al., 2021). The performance of fluorinated ILs in commercial packing columns for the separation of R-32 and R-134a (1,1,1,2-tetrafluoroethane) was assessed by Sosa et al., estimating an operation cost of 70 $/ton and 130 $/ton to recover 90% of R-134a and R-32, respectively, using 1-ethyl-3--methylimidazolium triflate (Sosa et al., 2020b).

In this context, adsorption processes have emerged as a high potential option, since they are already a mature industrial solution for several gas separations, such as the case of Pressure Swing Adsorption for oxygen production (Sircar and Kratz, 1989), hydrogen purification (Brea et al., 2019; Sircar and Golden, 2000), or biogas upgrading (Grande and Rodrigues, 2007). Temperature Swing Adsorption for the removal of volatile organic compounds (Bonjour et al., 2002; Yamauchi et al., 2007) and gas drying (Ahn and Lee, 2003; Ribeiro et al., 2011) are other examples of mature adsorption processes. Generally, the first step to assess the suitability of an adsorbent for a specific separation is to evaluate the adsorption equilibrium of the target species on a sample of the material. For this reason, in recent years several publications have reported the adsorption equilibria of F-gases on various adsorbents, namely activated carbons, zeolites, and metal-organic frameworks (MOFs). Askalany and co-workers studied the adsorption equilibrium (Askalany et al., 2013) and kinetics (Askalany and Saha, 2015) of R-32 over two activated carbons – Maxorb III and A-20 carbon fiber. Sosa et al. reported the adsorption equilibrium of R-32, R-125 and R-134a on four commercial activated carbons, showing suitable equilibrium selectivity for the separation of commercial refrigerant mixtures R-410A and R-407F (Sosa et al., 2020a).

In an early study regarding zeolites, Savitz et al. determined the adsorption equilibria and heats of adsorption of R-134 (1,1,2,2-tetrafluoroethane) and R-134a on a series of ion-exchanged (H, Li, Na, Rb, Cs) faujasites. R-134 was preferentially adsorbed on all the zeolites, except HY. The X-type zeolites showed higher selectivity than Y-type (Savitz et al., 1999). More recently, Fu et al. studied the competitive mechanism of chlorodifluoromethane (R-22) and trifluoromethane

(R-23) adsorption in faujasite zeolites (Fu et al., 2018) and Shifflet et al., studied the adsorption of R-23 on several zeolites – Na-Y, K,H-Y, Rb, Na-Y, 5A, LSX and 13X (Shiflett et al., 2013a, 2013b). More recently, Wanigarathna et al. reported the adsorption equilibrium of R-32, R-125, and R-22 on 4A zeolite, and also performed binary and ternary breakthrough curves, showing the potential of the adsorbent to separate R-32 and R-22 from R-125 due to steric effects (Wanigarathna et al., 2016). The adsorption of R-134a, R-125, and R-143a on 13X and modified 5A zeolites was also studied, showing that R-134a could be separated from R-125 and R-143a due to its preferential adsorption on zeolite 13X. The R-125/R-143a mixtures could be separated using a pore-size modified zeolite 5A which avoid the adsorption of R-143a, i.e. only retaining R-125 (Wanigarathna et al., 2018b). Yancey et al. explored the potential of LTA zeolites (3A, 4A, and 5A) for the adsorption of R-32 and R-125, observing the reversible adsorption of R-32 on zeolites 4A and 5A; the adsorption of R-32 on zeolite 3A also occurred but showed important kinetical limitations. The authors report irreversible R-125 adsorption on zeolite 5A, while its adsorption on 3A and 4A zeolites is negligible (Yancey et al., 2022a).

More recently, MOFs started to be considered for F-gases adsorption. Motkuri et al. evaluated the potential of four MOFs (MIL-101, MIL-100 (Fe), CoDOBDC, and NiDOBDC) for the adsorption of dichlorodifluoromethane (R-12), chlorotrifluoromethane (R-13), tetrafluoromethane (R-14), R-22, and R-32, concluding that the materials have good potential for the separation mixtures containing the said species (Motkuri et al., 2014). Zheng et al. studied the adsorption of R-134a on pore engineered Ni-MOF-74 MOFs, with promising results for adsorption cooling applications (Zheng et al., 2017). Wanigarathna at al. demonstrated the high uptake of UiO-66(Zr) towards R-22, R-125, and R-32 and its potential for their separation (Wanigarathna et al., 2018a). Sosa et al. determined the adsorption equilibrium of R-32, R-125 and R-134a on Cu-BTC, ZIF-8, MIL-53, and MOF-177, observing that all materials are selective for R-125 and R-134a at low pressures; the selectivity decreases with pressure, even switching to R-32 in some cases (Sosa et al., 2023).

Recently, Yancey et al. published an extensive review of adsorption equilibria data of F-gases (Yancey et al., 2022b). Nevertheless, to the best of our knowledge there are no studies available in the open literature regarding the design of continuous adsorption-based processes for the recovery of R-32 from refrigerant blends. A semi-continuous adsorption-based process, not yet fully described in the open literature due to IP policies, was developed in the KET4F-Gas European project (adsorption prototype). (KET4F-Gas, 2022)

Therefore, in this study we evaluate the feasibility of employing a Vacuum Swing Adsorption (VSA) process using activated carbon for the recovery of R-32 from the R-410A refrigerant blend (70 mol-% R-32 and 30 mol-% R-125). The single-component adsorption equilibria of R-32 and R-125 have been reported recently (Sosa et al., 2020a). Here, the adsorption kinetics of R-32 and R-125 are determined from dilute breakthrough experiments performed between 303 K and 345 K. The dynamic behavior of concentrated F-gas streams is studied using breakthrough experiments with higher adsorbate feed concentrations at 303 K and 1 bar. These data validate a simulation model that describes the breakthrough curves and predicts VSA cycles for the recovery of R-32 from R-410A blend.

2. Materials and methods

2.1. Materials

In this work coal-based activated carbon (AC) extrudates (Sutcliffe Speakman Carbons Ltd, U.K.) with 2 mm diameter were employed. The sample was selected due to its better R-32/R-125 selectivity in comparison with other carbons, as reported in a previous publication (Sosa et al., 2020a). The AC was extensively characterized; its main properties are reported in Table 1 and more details are reported elsewhere (Esteves et al., 2008). The F-gases employed in the experiments, R-32 (≥ 99.8% purity) and R125 (≥ 99.8% purity), were acquired from Polo Zero, while helium (≥ 99.999% purity) was purchased from Air Liquide.

Table 1
Adsorbent and fixed-bed properties.

Adsorbent properties (Esteves et al., 2008)		Fixed-bed properties (Ribeiro et al., 2017)	
Specific pore volume, V_μ (cm^3/g)	0.860	Bed length, L (cm)	18.0
BET surface area, A_{BET} (m^2/g)	1342	Bed diameter, d_c (cm)	2.1
Particle density, ρ_p (g/cm^3)	0.763	Adsorbent weight (g)	25.75
Intraparticle void fraction, ε_p (-)	0.656	Bed porosity, ε_c (-)	0.459
Mean particle radius, r_p (mm)	1.07	Bulk density, ρ_b (g/cm^3)	0.413

The experiments were performed using a cylindrical fixed-bed with length of 18 cm and internal diameter of 2.1 cm packed with the AC. The fixed-bed properties are given in Table 1; more details can be found in a previous publication using the same packed bed (Ribeiro et al., 2017). Prior to each breakthrough curve the adsorbent bed is regenerated by heating to 363 K under vacuum for 9 h.

2.2. Diluted breakthrough experiments

The adsorption kinetics of R-32 and R-125 were studied by analysis of dilute breakthrough curves performed using helium as carrier gas. Experiments with trace compositions (0.5 − 1% for R-32 and 0.25−0.5% for R-125, both balanced with He) were performed at three different temperatures, namely 303, 323, and 345 K, as the adsorption equilibrium has also been previously measured at 303 and 323 K (Sosa et al., 2020a). The experiments were performed with the total pressure of the system fixed at 4 bar to control the velocity inside the fixed-bed, while generating the desired feed concentrations with the mass flow controllers available at the experimental apparatus. Twelve breakthrough curves and their respective desorption curves were performed; the latter were obtained by purging the fixed-bed with He. The conditions employed in the experiments are summarized in Tables 2.

2.3. Concentrated breakthrough experiments

Breakthrough experiments with bulk feed concentration were performed to validate the mathematical model using the previously determined kinetics parameters and to calibrate the heat transfer parameters of the system. For this purpose, breakthrough curves were firstly obtained by feeding pure F-gas (R-32 or R-125) balanced with He, at 1 bar and 303 K as this are the feed conditions of the VSA process under study. Binary mixtures of R-32/R-125 generated by mixing the pure gases were also studied and the results compared with breakthrough curves for a commercial R-410A blend (30 mol-% R-125 / 70 mol-% R-32). The conditions employed are shown in Table 3.

2.4. Vacuum swing adsorption validation

VSA operation was validated experimentally by running the four-step example cycle shown in Fig. 1 using our single-column system. The feed pressure and flowrate were 1.01 bar and 0.350 slpm, respectively; the lower pressure of the cycle was defined as 0.1 bar as this is a

Table 2
Experimental conditions employed in the diluted breakthrough curves. The purge molar flowrate is the same as used in the feed.

Adsorbate	T (K)	$y_{i,feed}$ (mol-%) RUN 1	$y_{i,feed}$ (mol-%) RUN 2	F_{feed} (mmol/s)
R-32	303	0.97	0.49	1.8
	323	1.03	0.52	1.7
	345	1.09	0.56	1.6
R-125	303	0.46	0.23	1.8
	323	0.49	0.25	1.7
	345	0.52	0.26	1.6

Table 3
Experimental conditions employed in the bulk breakthrough curves at fixed pressure and temperature of 1.01 bar and 303 K, respectively. The purge molar flowrate is the same as used in the feed.

Run	$y_{i,feed}$ (mol-%)		F_{feed} (mmol/s)
1	48.8 (R-32)	51.2 (He)	0.261
2	47.8 (R-125)	52.2 (He)	0.269
3	49.8 (R-32)	50.2 (R-125)	0.256
4	68.4 (R-32)	31.6 (R-125)	0.249
5	100 (R-410A)		0.256

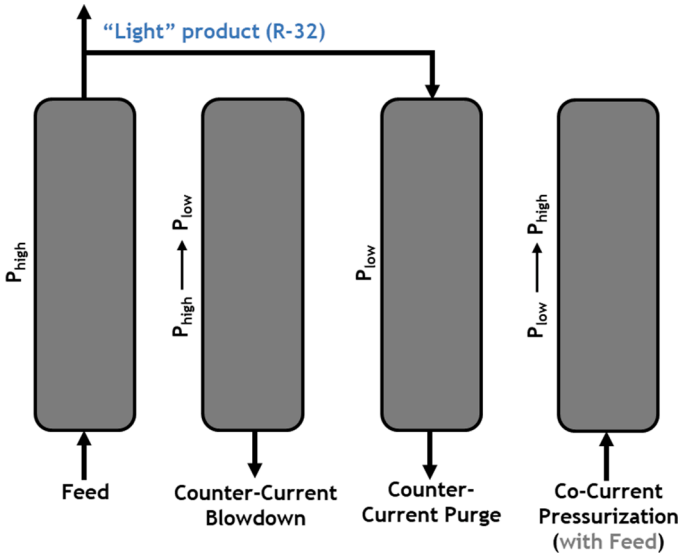

Fig. 1. Four-step VSA cycle: feed, counter-current blowdown (B), Counter-current purge (P), Co-current pressurization (Press).

typically value employed in VSA processes. Table 4 lists the full set of experimental conditions.

3. Theoretical

In this work breakthrough curves were performed using the adsorbate under dilute and bulk feed conditions. The diluted breakthrough curves use a single adsorbate (R-32 or R-125) balanced with He, while in the case of the concentrated breakthrough curves, both single and binary adsorbate feed compositions were employed.

A simulation model that describes both types of experiments was developed. The general assumptions of the model are (i) ideal gas behavior, (ii) constant porosity along the bed, (iii) no cross-sectional mass, heat, or velocity gradients, (iv) linear driving force (LDF) model to describe lumped solid-diffusion mass transfer, and (v) axially dispersed plug flow. The model consists of mass, momentum and energy balances to describe the dynamic behavior along the axial axis of the column (Da Silva et al., 1999).

The differential material balance for the *i*th component of the gas mixture can be written as

$$\frac{\partial C_i}{\partial t}+\left(\frac{1-\varepsilon_c}{\varepsilon_c}\right)\rho_p\frac{\partial \overline{q}_i}{\partial t}=\frac{\partial}{\partial z}\left(D_z C_t\frac{\partial y_i}{\partial z}\right)-\frac{\partial(vC_i)}{\partial z} \tag{1}$$

where C_i is the gas concentration at axial position z and instant t, ε_c the bed porosity, ρ_p the density of the activated carbon extrudates, $\overline{q}_i$ the average amount adsorbed, v the interstitial velocity ($u=\varepsilon_c v$ is the superficial velocity), C_t the total concentration ($C_t=\sum C_i$), y_i the mole fraction, and D_z the axial dispersion coefficient.

The lumped solid-diffusion LDF model can be written as

$$\frac{\partial \overline{q}_i}{\partial t}=k_{LDF,i}\left(q_i^*-\overline{q}_i\right) \tag{2}$$

where $k_{LDF,i}$ is the LDF coefficient for component i and q_i^* the equilibrium loading of component i. The temperature dependence of the LDF coefficient is approximated as

$$k_{LDF,\,i}=k_{LDF,i}^0\exp\left(\frac{-E_{a,i}}{R_g T}\right) \tag{3}$$

where $k_{LDF,i}^0$ is the limiting value of the LDF coefficient at infinite temperature, $E_{a,i}$ an activation energy, R_g the ideal gas constant, and T the system temperature.

The adsorption equilibrium is described by the multicomponent extension of the dual-site Langmuir model, expressed as

$$q_i^*=q_{1,i}^\infty\frac{b_{1,i}P_i}{1+\sum_{j=1}^n b_{1,j}P_j}+q_{2,i}^\infty\frac{b_{2,i}P_i}{1+\sum_{j=1}^n b_{2,j}P_j} \tag{4}$$

$$b_{k,i}=b_{k,i}^0\exp\left(\frac{-\Delta H_{k,i}}{R_g T}\right), \tag{5}$$

where $q_{1,i}^\infty$ and $q_{2,i}^\infty$ are the saturation capacities, $b_{1,i}$ and $b_{2,i}$ the affinity constants, and P_i the partial pressure; $-\Delta H_{k,i}$ is the heat of adsorption and $b_{k,i}^0$ the affinity constant at infinite temperature for each site k.

The momentum balance is given by the Ergun equation,

$$-\frac{\partial P}{\partial z}=\alpha\mu_g v+\beta\rho_g|v|v,\ \alpha=\frac{150(1-\varepsilon_c)^2}{\varepsilon_c^2 d_p^2},\ \beta=\frac{1.75(1-\varepsilon_c)}{\varepsilon_c d_p}, \tag{6}$$

where μ_g is the gas viscosity, ρ_g the gas density, and d_p the diameter of the adsorbent pellets. It is unfortunate that it has gone unnoticed in most of the open literature that this equation can be rewritten explicitly as a function of v as follows (Mota et al., 1995)

$$v=-\frac{2}{\alpha\mu_g+\sqrt{(\alpha\mu_g)^2+4\beta\rho_g\left|\frac{\partial P}{\partial z}\right|}}\frac{\partial P}{\partial z}. \tag{7}$$

Substituting this equation into the material and energy balances eliminates the velocity, $v(z,t)$, as dependent variable from the model, leaving only the axial pressure profile, $P(z,t)$, as unknown. This makes the model easier to solve numerically.

The temperature changes across the column are described through two energy balances: one for the fixed-bed and one for the column wall. The energy balance of the fixed-bed lumps the solid and gas phase, considering that the adsorbent is in local thermal equilibrium with the gas phase. The gas/solid adsorbent energy balance is described by

$$\begin{aligned}&\left[\varepsilon_c\sum_{i=1}^n C_i\widetilde{C}_{g,i}+(1-\varepsilon_c)\left(\rho_p\sum_{i=1}^n\overline{q}_i\widetilde{C}_{g,i}+\rho_p\widetilde{C}_s\right)\right]\frac{\partial T}{\partial t}\\&-\rho_b\left(\sum_{i=1}^n(-\Delta H_i)\frac{\partial \overline{q}_i}{\partial t}\right)\\&=\frac{\partial}{\partial z}\left(\lambda\frac{\partial T}{\partial z}\right)-\varepsilon_c v\sum_{i=1}^n C_i\widetilde{C}_{g,i}\frac{\partial T}{\partial z}+\varepsilon_c R_g T\frac{\partial C_t}{\partial t}-\frac{2}{r_c}h_{cw}(T-T_w)\end{aligned} \tag{8}$$

Table 4
Experimental conditions employed in the VSA cycle. Pressures (P) are reported in bar, flowrates (Q) in slpm, and step durations (t) in seconds.

P_{high}	P_{low}	Q_{feed}	Q_{purge}
1.01	0.10	0.335	0.176
t_{feed}	t_{blow}	t_{purge}	t_{press}
230	80	100	180

where λ is the effective thermal conductivity of the fixed bed, $\widetilde{C}_{g,i}$ the molar specific heat of component i, r_c the inner radius of the cylindrical column, h_{cw} the heat transfer coefficient between adsorption bed and column wall, T_w the column wall temperature, $\widetilde{C}_s$ the adsorbent specific heat, and ρ_b the bulk density of the adsorption bed.

The energy balance at the stainless-steel column wall is

$$\rho_w \widetilde{C}_w \frac{\partial T_w}{\partial t} = \alpha_w h_{cw}\left(T_g - T_w\right) - \alpha_{wl} U (T_w - T_\infty), \tag{9}$$

where ρ_w, $\widetilde{C}_w$, and T_w are, respectively, the density, specific heat, and temperature of the column wall; U is the overall heat transfer coefficient, T_∞ the external environment temperature, α_w and α_{wl} are the ratio of the internal surface area to the column wall volume and the ratio of the logarithmic mean surface area of the column shell to the volume of the column wall, respectively (Ribeiro et al., 2011).

The boundary and initial conditions employed to simulate the breakthrough experiments and VSA cycles, as well as the correlations used for calculating the heat and mass transfer parameters employed in the mathematical model are indicated in the S.I. file, except for h_w and U which were obtained from the fitting of the concentrated experimental breakthrough curves. The equations were discretized along the axial coordinate using the third-order centred finite differences method (CFDM) with a uniform grid of 30 intervals, and integrated over time using gPROMS 4.0.0 (PSE-Siemens, U.K.).

The particular case of experimental breakthrough curves generated with adsorbate at very low concentration (0.25−1%) diluted in helium is analyzed using a simplified version of the model. Under dilute experimental conditions the solid adsorbs only small percentages of the feed stream, so changes in temperature and fluid velocity along the adsorption bed are negligible, i.e., the momentum and energy balances can be dropped from the model.

4. Results and discussion

4.1. Dilute breakthrough curves

Dilute breakthrough curve experiments of R-32 and R-125 were performed at three temperatures (303 K, 323 K, and 345 K) and two feed concentrations (0.25–1%). The breakthrough curves, and corresponding desorption curves, at the three temperatures and feed concentration of ca. 0.5% are plotted in Fig. 2 for R-32 and in Fig. 3 for R-125. The remaining dilute breakthrough curves are shown in the Supporting Information file. As stated above, the dilute breakthrough curves were obtained under near isothermal conditions, so this simplification was considered in the model Eqs. (1)–(5). In Figs. 2 and 3 the solid lines represent the simulations that best fit the k_{LDF} parameter to each experimental curve; the results show that the model describes the experimental data accurately. The LDF constants obtained from the fitting follow an Arrhenius-type temperature dependence (Eq. (3)), as demonstrated in Fig. 4. The fitted parameters are reported in Table 5; their values were subsequently employed in the simulations of higher concentration breakthrough curves and VSA cycles.

4.2. Concentrated breakthrough curves

After obtaining the kinetic parameters from the diluted breakthrough curves, further experiments were performed at 303 K using more concentrated feed streams (~50 mol-% of R-32 or R-125 in helium). Fig. 5(a) and (c) show, respectively, the experimental and simulated concentrations of R-32 and R-125 exiting the column for the breakthrough curves with HFC feed concentrations of 48.8% (R-32) and 47.8% (R-125). The adsorption equilibrium is described by the dual-site Langmuir model. The simulations describe well the dynamic behavior of the concentration fronts in the adsorption bed for the concentrated breakthrough experiments. Furthermore, the temporal temperature profiles at three axial positions (z = 0.045, 0.090, and 0.135 m) inside the column are also successfully described by the mathematical model (additional information available in the S.I. file).

The experiments shown in Fig. 5 demonstrate that the simulation model successfully describes the breakthrough curves and temperature changes when the column is feed with a single concentrated HFC. The desorption curves are also successfully described by the model.

Subsequently, experiments with binary mixtures of R-32 and R-125 were performed to evaluate whether the simulation model based on the dual-site Langmuir model successfully describes the multicomponent adsorption data and mixed-feed streams. The results are shown in Fig. 6, for R-32/R-125 feed mixtures of 49.8 mol-%/50.2 mol-% (a, b) and 68.4 mol-%/31.6 mol-% (c, d); the latter corresponds to a feed composition similar to commercial R-410A (70 mol-% R-32 and 30 mol-% R-125). Again, both experiments are very well described by the simulation model, both in terms of outlet molar fraction and temperature history within the fixed-bed. Details of the temperature history for each axial position can be seen in the S.I. file for the breakthrough experiment with feed composition of 49.8 mol-% R-32 / 50.2 mol-% R-125, highlighting the very good fitting obtained. The results demonstrate that the multicomponent adsorption is successfully described by the classical extension of the adsorption equilibrium data obtained from the pure-component isotherms; furthermore, the LDF parameters determined for the pure components allow a good prediction of the mass transfer under multicomponent conditions. The heat transfer parameters, h_{cw} (80 W m^{-2} K^{-1}) and U (25 W m^{-2} K^{-1}), which are used next for the simulation of VSA cycles, were obtained by fitting the simulation model to the multicomponent breakthrough experiments.

Finally, a breakthrough experiment (Run 5) using R-410A (70 mol-% R-32 / 30 mol-% R-125) was performed and compared with the

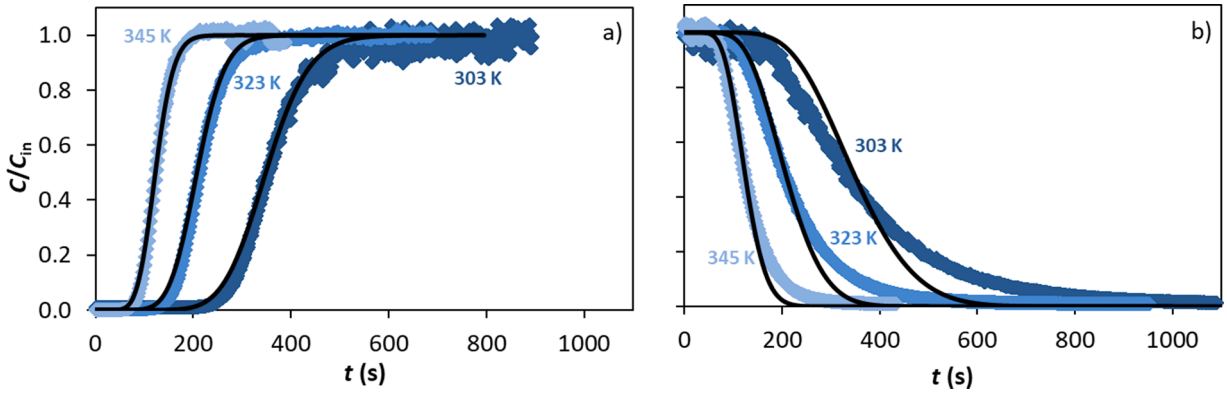

Fig. 2. (a) R-32 dilute breakthrough curves and (b) purge with helium at 303 K, 323 K, and 345 K for $y_{feed,R-32}$ = 0.49%, 0.52% and 0.56%, respectively. The solid lines represent the model fit.

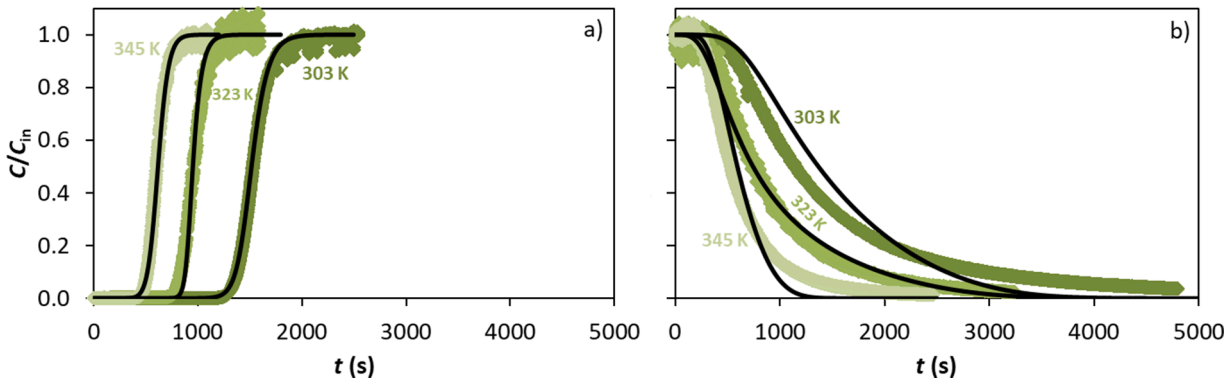

Fig. 3. (a) R-125 dilute breakthrough curves and (b) purge with helium at 303 K, 323 K, and 345 K for $y_{feed,R-125}$ = 0.46%, 0.49% and 0.52%, respectively. The solid lines represent the model fit.

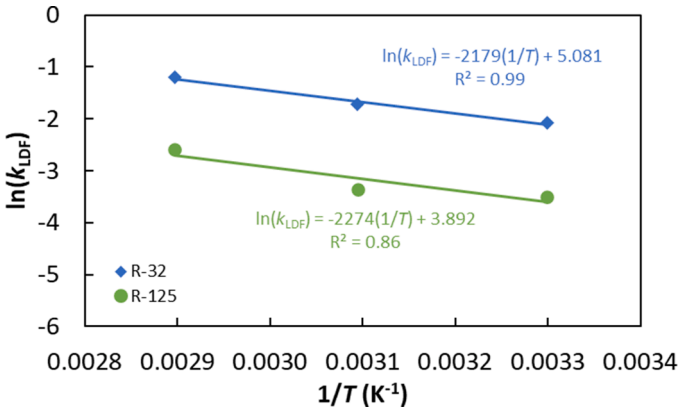

Fig. 4. Temperature dependence of the LDF coefficients for R-32 and R-125 adsorption on the activated carbon between 303 K and 345 K.

Table 5
LDF coefficients for R-32 and R-125 adsorption on the activated carbon at 303 K, 323 K, and 345 K.

Gas	T (K)	k_{LDF} (s^{-1})	k^0_{LDF} (s^{-1})	E_a (kJ/mol)
R-32	303	0.125	160.9	18.1
	323	0.180		
	345	0.300		
R-125	303	0.030	49.0	18.9
	323	0.035		
	345	0.075		

breakthrough experiment (Run 4) which employs a similar composition prepared in our experimental fixed-bed apparatus from the mixing of two streams of pure R-32 and R-125. The experimental results obtained confirm that both breakthrough curves are similar, regardless of using the commercial blend or an in-house prepared mixture (Supporting Information). This allows to confidently extrapolate our results to the separation of R-410A in real scenarios.

4.3. Vacuum swing adsorption experimental validation

The various experimental breakthrough curves allowed to calibrate the model parameters for predicting the system behavior in a cyclic separation process. Therefore, a VSA cycle was experimentally run to evaluate whether the simulation model using the extracted mass and heat transfer parameters predicts the experimental behavior. For this purpose, the simple four-step Skarström-like VSA cycle described in Fig. 1 was employed. It should be noted that in this work only one column is used, and purge with light product is performed using a pure R-32 stream. The experimental conditions and step durations are described in Table 4. For the purposes of experimental validation, eight cycles were performed, starting with the fixed-bed filled with inert. The experimental (symbols) and simulated (lines) results are shown in Fig. 7.

The experimental pressure is very well predicted by the simulation model, as shown in Fig. 7(a) for the eight VSA cycles and detailed in Fig. 7(b) for cycles 7 and 8. The experimental and simulated outlet molar fractions of R-32 and R-125 are compared in Fig. 7(c, d), showing that the simulations predict very well the experimental results. Fig. 7(d) shows that, although there is some difference between predictions and experiments in the low-pressure steps (blowdown and purge), the mole fraction exiting the column during the feed step is perfectly predicted. The latter step (feed) is the one during which R-32 is obtained; therefore, our calculations of process performance (purity, recovery, etc.) are perfectly reliable. Finally, Fig. 7(e, f) compares simulations with the temperature measurements at axial positions 0.045, 0.090, and 0.135 m from the bed inlet. Once again, the results show a good fit between experiments and predictive calculations, demonstrating the robustness of our mathematical model and parameters employed.

4.4. Vacuum swing adsorption simulations

The confirmation that our process simulation results can predict the experimental VSA results, enable the study of each cycle step influence in the process performance. For this purpose, the feed/exterior temperature is fixed at 303 K, the feed pressure at 1.01 bar, the feed flowrate at 0.350 slpm, and the purge flowrate at 0.125 slpm; the VSA cycle is that depicted in Fig. 1. Process performance is evaluated using typical parameters, namely, R-32 purity and recovery, unit productivity and energy consumption, all calculated under cyclic steady-state (CSS) conditions which are reached rather quickly (typically between the fifth and seventh cycles). The R-32 purity is determined from the individual molar flow rate of each component exiting the column during the feed step:

$$\text{Purity}_{R-32} = \frac{\int_0^{t_{feed}} F^{out}_{R-32}\,dt}{\int_0^{t_{feed}} F^{out}_{R-32}\,dt + \int_0^{t_{feed}} F^{out}_{R-125}\,dt}, \tag{10}$$

where $F_i^{out}(t)$ is the outlet individual molar flowrate of component i. The R-32 recovery is determined as the ratio of moles obtained in the feed step after discounting the moles spent in the purge step, and dividing it by the number of moles that enter the column (during the feed and pressurization steps):

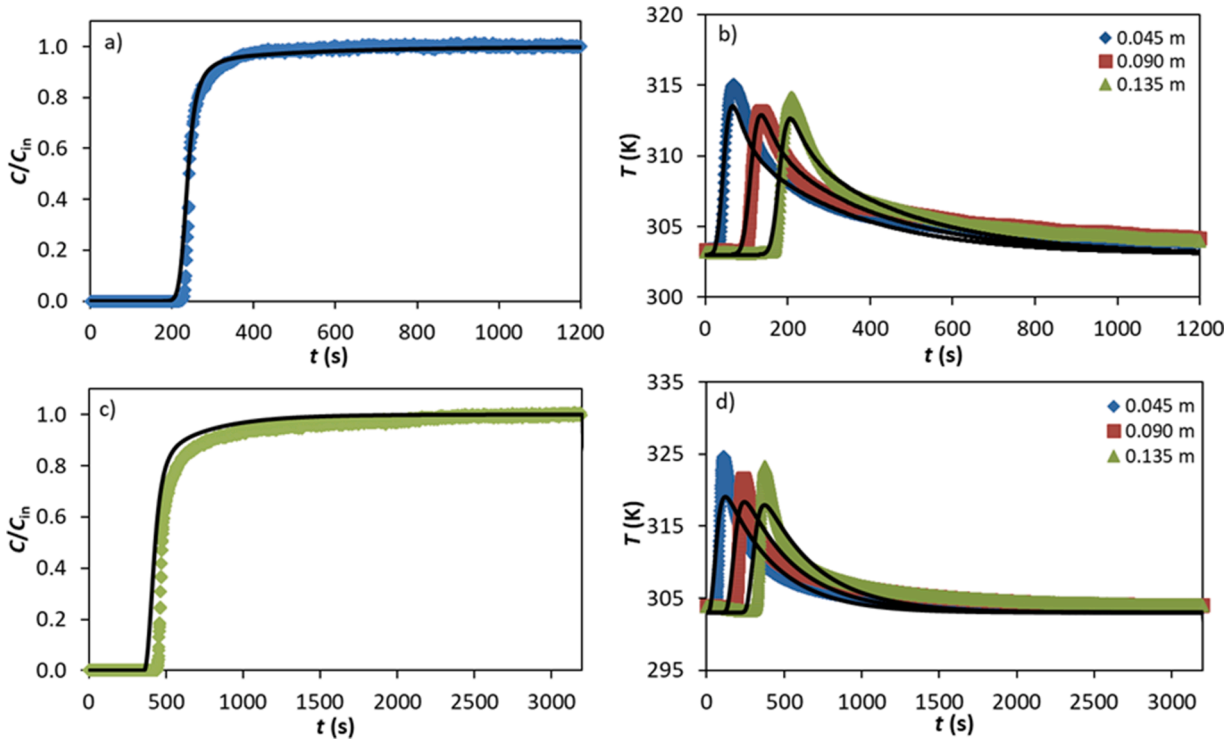

Fig. 5. (a) R-32 and (c) R-125 normalized outlet concentration during a breakthrough experiment performed at 303 K, 1.01 bar of total pressure, and HFC feed mole fraction $y_{feed,R-32} = 48.8\%$ and $y_{feed,R-125} = 47.8\%$, balanced with He; (b) and (d) represent the temperature history measured at axial positions 0.045 m, 0.090 m, and 0.135 m from the feed inlet, for the R-32 and R-125 breakthrough experiments, respectively. Solid lines represent the simulation results.

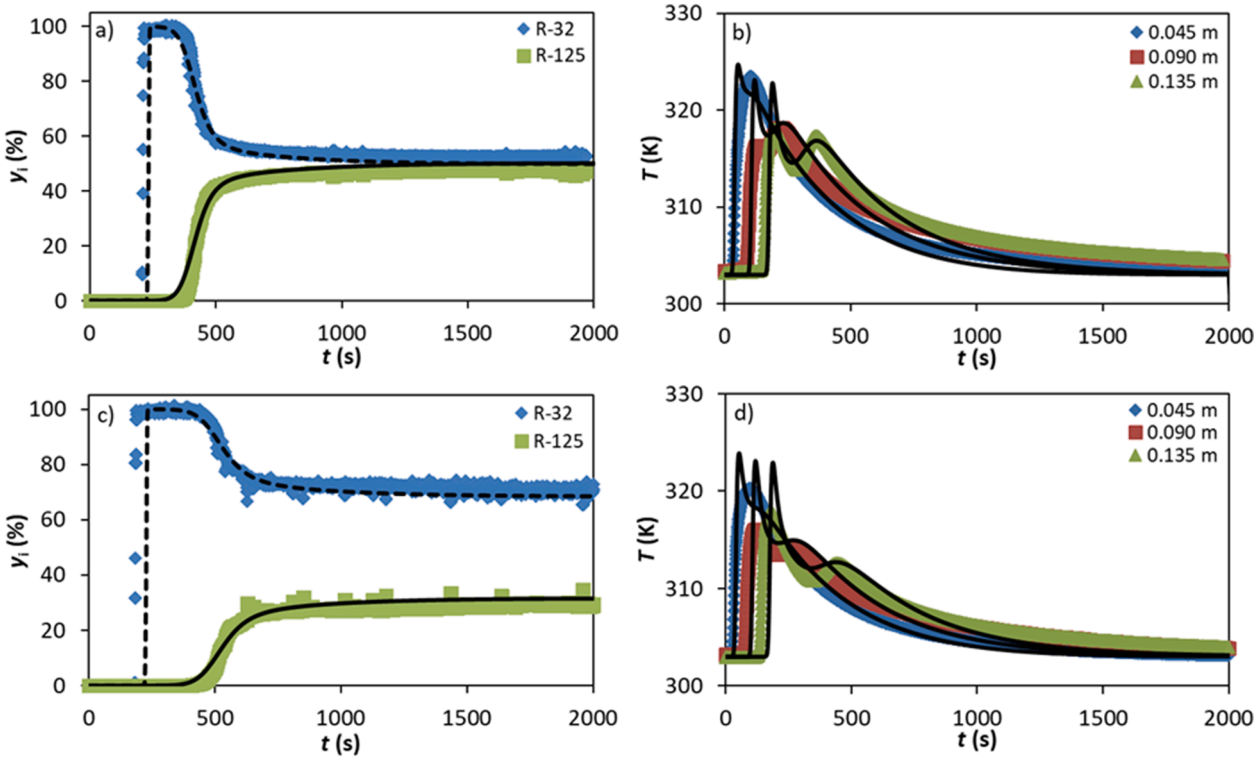

Fig. 6. (a) R-32 and R-125 outlet concentrations and (b) temperature history at 0.045, 0.090, and 0.135 m from the feed inlet, for a breakthrough experiment with $y_{feed,R-32} = 49.8\%$ and $y_{feed,R-125} = 50.2\%$. (c) R-32 and R-125 outlet concentrations and (d) temperature history at axial positions 0.045 m, 0.090 m, and 0.135 m from the feed inlet, for a breakthrough experiment performed with $y_{feed,R-32} = 68.4\%$ and $y_{feed,R-125} = 31.6\%$. Solid lines represent the simulation results.

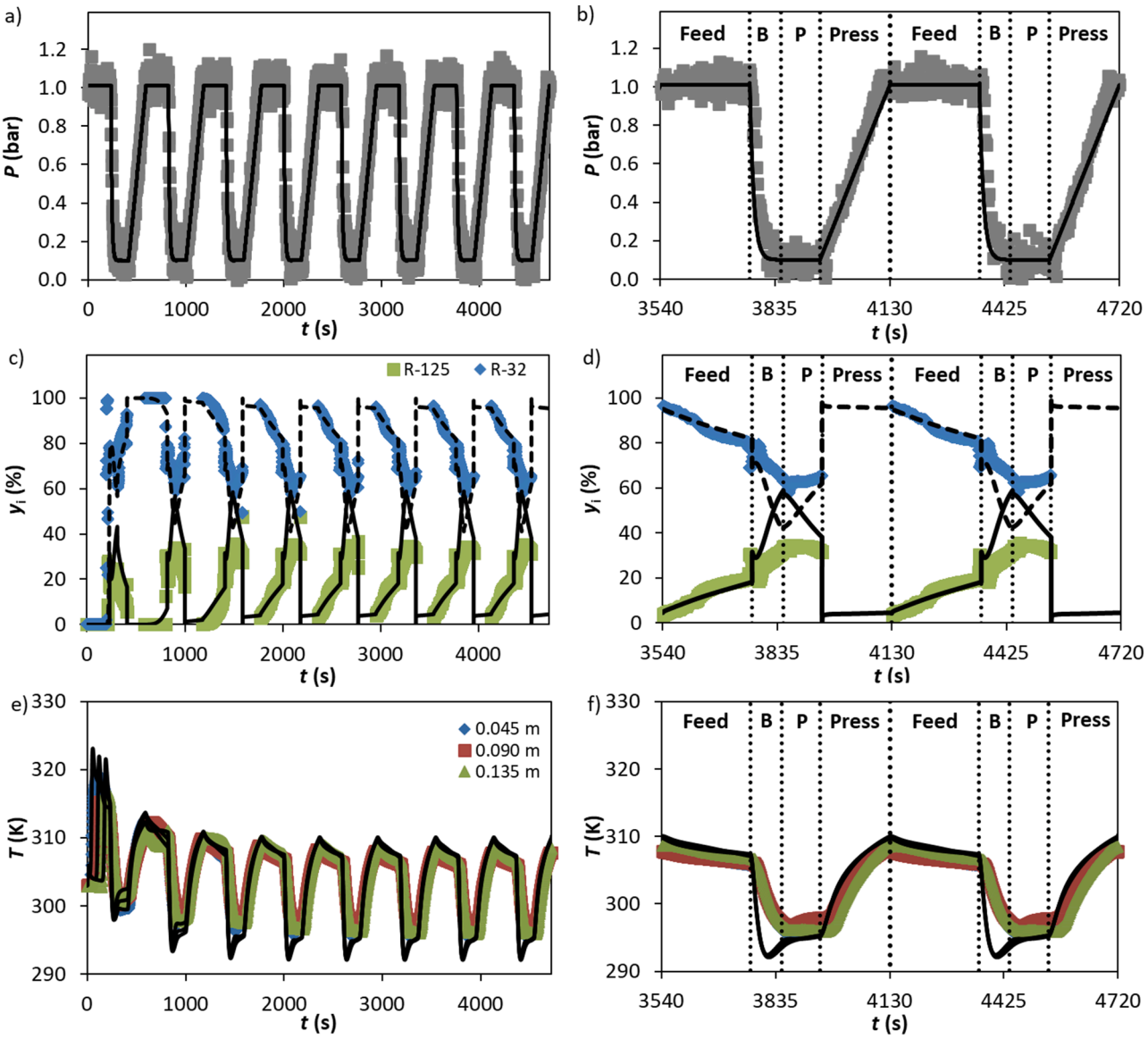

Fig. 7. (a) Outlet pressure, (c) R-32 and R-125 outlet molar fraction, and (e) temperature histories (at axial positions $z = 0.045, 0.090, 0.135$ m) during eight VSA cycles performed experimentally. The outlet pressure, outlet molar fraction, and temperature histories of cycles 7 and 8 are showed with detail in (b), (d), and (f), respectively. The symbols represent the experimental data and the solid lines the simulation.

$$\text{Recovery}_{R-32} = \frac{\int_0^{t_{feed}} F_{R-32}^{out} dt - \int_0^{t_{purge}} F_{R-32}^{in} dt}{\int_0^{t_{feed}} F_{R-32}^{in} dt + \int_0^{t_{press}} F_{R-32}^{in} dt} \quad (11)$$

where $F_i^{in}(t)$ is the inlet individual molar flowrates of component i.

The productivity is calculated as the amount of R-32 processed per unit amount of adsorbent and per unit time:

$$\text{Productivity}_{R-32} = \frac{\int_0^{t_{feed}} F_{R-32}^{out} dt - \int_0^{t_{purge}} F_{R-32}^{in} dt}{\rho_b V_c t_{cycle}} \quad (12)$$

The energy consumption in the vacuum-using steps (blowdown and purge) is estimated as follows:

$$\text{Energy}_{R-32} = \frac{\int_0^{t_{blow+purge}} \text{Power}_{vac} dt}{\int_0^{t_{feed}} F_{R-32}^{out} dt - \int_0^{t_{purge}} F_{R-32}^{in} dt} \quad (13)$$

$$\text{Power}_{vac} = \frac{1}{\eta} \frac{\gamma}{\gamma - 1} R_g T_{blow} \left[\left(\frac{P_{atm}}{P_{blow}} \right)^{\frac{\gamma}{\gamma-1}} - 1 \right] u^{out} A_c \frac{P_{blow}}{R_g T_{blow}} \quad (14)$$

where γ is the ratio between the constant pressure and constant volume specific heats and η is the isentropic efficiency (herein assumed as 0.8). It should be noticed that this approach does not consider the eventual energy needs to compress the obtained R-32 product.

The experimental conditions for each cycle simulated and the process performance results obtained at CSS are shown in Table 6. First, the blowdown/purge pressure of the cycle was fixed at 0.1 bar and nine VSA cycles were performed using different step durations, except for the pressurization step which was kept constant in all simulations ($t_{press} = 200$ s). As can be seen, the obtained purity for this regeneration pressure is quite low and the recovery results are also very modest; for example, the recovery is only 21.4% for the maximum purity obtained (96.1 mol-%). This means that the results of the trade-off between purity and recovery are very limited under these conditions: i.e., R-32 purities greater than 96% are only obtained with very low recovery values. Therefore, the possibility of using a regeneration pressure of 0.01 bar was evaluated

Table 6
Conditions employed in the VSA simulations and calculated R-32 purity, recovery, productivity, and energy consumption.*

Run	P_{low} (bar)	t_{feed} (s)	t_{blow} (s)	t_{purge} (s)	Purity (mol-%)	Recovery (%)	Productivity (mol kg^{-1} h^{-1})	Energy (kJ mol^{-1})
1	0.1	200	60	200	93.1	33.6	4.88	34.2
2		200	200	200	93.9	33.6	4.03	34.4
3		200	400	200	94.2	33.5	3.21	34.6
4		200	600	200	94.3	33.4	2.67	34.7
5		200	800	200	94.3	33.4	2.29	34.8
6		200	200	180	93.1	36.0	4.42	31.2
7		200	200	150	91.6	39.6	5.03	27.1
8		180	600	200	95.0	28.0	3.24	43.9
9		150	600	200	96.1	21.4	2.38	61.2
10	0.01	200	60	200	95.9	30.9	4.92	122
11		200	200	200	97.0	30.9	4.06	123
12		200	400	200	97.3	30.8	3.23	124
13		200	600	200	97.4	30.7	2.68	124
14		200	800	200	97.4	30.7	2.30	124
15		200	200	180	96.6	33.3	4.49	112
16		200	200	150	96.0	36.9	5.16	96.9
17		175	200	200	97.7	25.4	3.24	158
18		150	200	200	98.3	19.0	2.35	223

* The pressurization time is 200 s in all cycles.

as a way to improve process performance. For this purpose, nine more VSA cycles were simulated (Table 6) and it was observed that the performance obtained benefited significantly from the decrease in the vacuum pressure used. For example, by lowering the regeneration pressure to 0.01 bar the maximum purity obtained was 98.3 mol-% while the recovery was only slightly affected (decreased from 21.4% at 0.10 bar to 19.0% at 0.01 bar).

By comparing in more detail the VSA cycles of runs 2 and 11, which differ only in the regeneration pressure and are both stepwise symmetrical (all four steps of the cycle have the same duration), the influence of the regeneration pressure can be analysed. Fig. 8 shows the CSS histories of pressure (a), temperature (b), and outlet molar flowrate (c) for VSA runs 2 and 11. The change in the regeneration pressure promotes a slightly wider swing between the high and low temperatures occurring during the cycle. It also changes the outlet composition during the blowdown, purge, and, more importantly, during the feed step. Lowering the regeneration pressure to 0.01 bar during blowdown ensures better clean-up of the column, as demonstrated by the higher outlet molar flowrates of both R-32 and R-125, than when the regeneration pressure is 0.1 bar. Fig. 8(d) shows in detail the outlet streams obtained during the feed step, which is the R-32 producing step. It is clearly observed that the R-125 molar flowrate exiting the column in this step decreases when a lower pressure is used to regenerate the column. This results in a purity increase from 93.9 mol-% to 97.0 mol-% when the regeneration pressure is decreased from 0.1 to 0.01 bar. This clearly demonstrates the impact of using a lower vacuum pressure on the R-32 purity obtained; however, the recovery is still limited to 30.9%.

Fig. 9 shows the axial concentration profiles of R-32 and R-125 in the solid and gas phases, as well as the temperature profile, all under CSS conditions, at the end of each step of the Run 11simulated VSA cycle. Fig. 9(a) shows that at the end of the feed step there is still a significant amount adsorbed of each of HFC, as a result of the limited selectivity of the adsorbent. Furthermore, at the end of the blowdown and purge steps, the amount of R-32 still adsorbed is negligible, while there is still

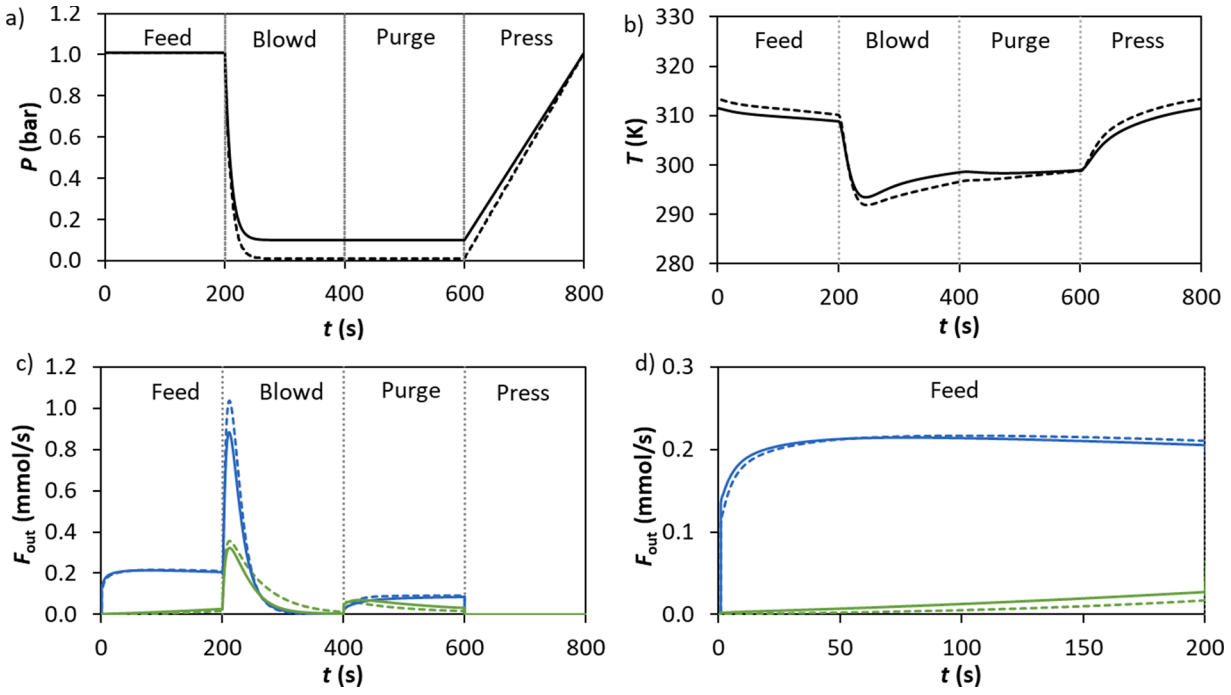

Fig. 8. (a) Pressure, (b) temperature (at $z = 0.09$ m), and (c) R-32 (blue) and R-125 (green) outlet molar flowrate history at CSS for the VSA cycles of Run 2 (solid lines) and Run 11 (dashed lines). In (d) the outlet molar flowrate during the feed step is showed in more detail.

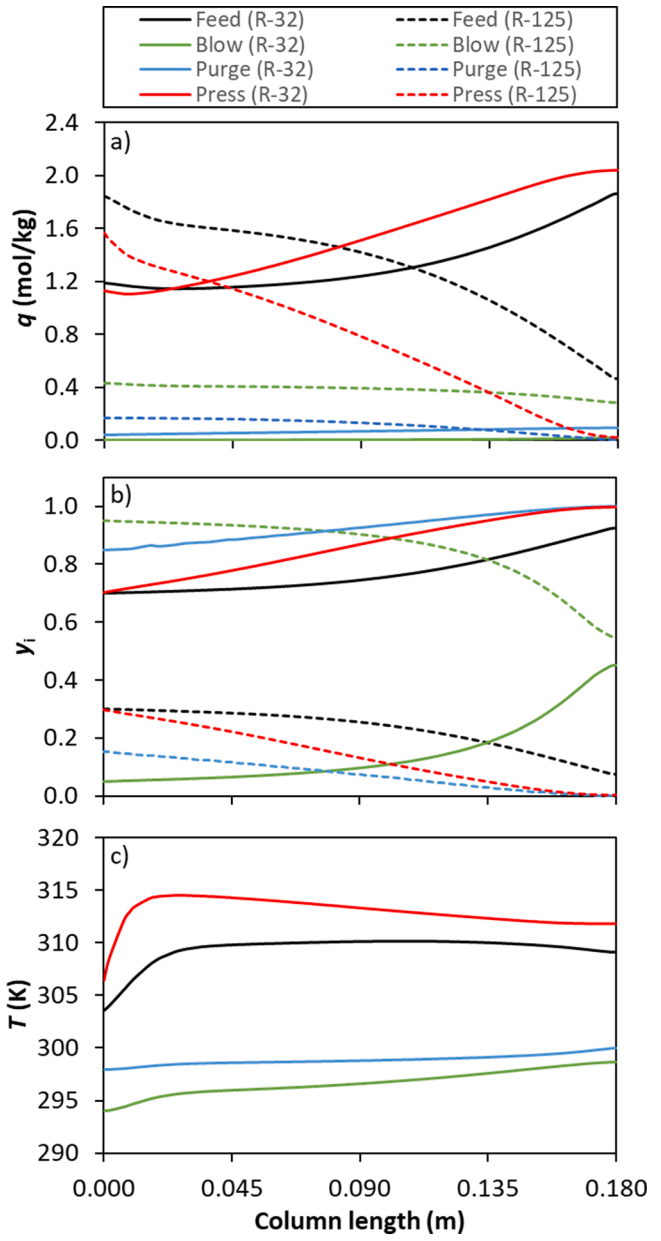

Fig. 9. Simulated internal profiles at the end of each step of VSA Run 11 at CSS: (a) amount adsorbed of R-32 and R-125; (b) gas-phase molar fraction of R-32 and R-125; (c) temperature.

some R-125 adsorbed and spread over almost the entire length of the column.

Fig. 9(b) shows the mole fraction of each species in the gas phase at the end of each step. The results clearly indicate that the only time a part of the column is clean of R-125 is at the end of the purge step and only in a small region near the end of the column (through which the purge is being fed). For this reason, large amounts of the light component (R-32) are spent in the purge, limiting the recovery of this species.

Fig. 9(c) shows the CSS temperature profiles at the end of each step. The step at which the fixed bed reaches the lowest temperature is the blowdown step (294–298 K); then, during the purge step a slight temperature increase is observed (298 – 300 K). In the pressurization step there is a much larger temperature increase over the entire length of the column, due to the effects of increased pressure and adsorption of the fed species. Finally, at the end of the feed step a temperature decrease is observed throughout the column (this can be seen in Fig. 9c and is in agreement with Fig. 8(b) and the experimental observations in Fig. 7(f).

In the VSA cycles reported here a temperature increase due to the heat released by the adsorption of the heavy species in the feed step is not observed experimentally nor in the simulations. To analyse this observation, the influence of each term in the energy balance (Eq. (8)) was evaluated and it was concluded that the dominant terms are the heat generated due to adsorption/desorption, $\rho_b \sum_{i=1}^{n}(-\Delta H_i)\frac{\partial \bar{q}_i}{\partial t}$, and the heat transfer across the column wall, $-2h_{cw}/r_c(T-T_w)$. Fig. 10(b) shows the sum of both terms, Heat Power $= \rho_b \sum_{i=1}^{n}(-\Delta H_i)\frac{\partial \bar{q}_i}{\partial t} - 2h_{cw}/r_c(T-T_w)$, at the fixed axial position in the column $z = 0.09$ m. Fig. 10(a) also shows the temporal profiles of the adsorbed amounts of R-32 and R-125 and the temperature profile at the same axial position. In the pressurization step both species are adsorbed and therefore the *Heat Power* is positive, which means that the heat released is higher than the energy transferred to the column wall—this results in a temperature increase. On the other hand, in the feed step, although R-125 (heavier species) is adsorbed, there is a significant quantity of R-32 desorbed at the same time. The net effect is a slight decrease in bed temperature, since the heat released by the adsorption of R-125 does not compensate for the heat consumed in the desorption of R-32 plus the energy losses to the column wall.

Finally, Fig. 11 shows plots of R-32 purity as function of recovery and energy spent in vacuum steps for the set of VSA cycles simulated and detailed in Table 6. The results clearly demonstrate that lowering the regeneration pressure increases the purity of the VSA cycle, but the recovery remains constrained: all recovery values fall below 40%. The higher recovery rates are 39.6% (purity of 91.6 mol-%) when the adsorbent is regenerated at 0.1 bar, and 36.9% (purity of 96.0 mol-%) at 0.01 bar. Additionally, Fig. 11(b) shows the increased energy consumption (considering only the vacuum pump) required to achieve higher R-32 purity.

Overall, this first study focusing on the application of VSA for the recovery of F-gases demonstrated that this technology has the potential to be viewed as an option for the continuous production of high-purity R-32 from R-410A blend. Furthermore, there is room for

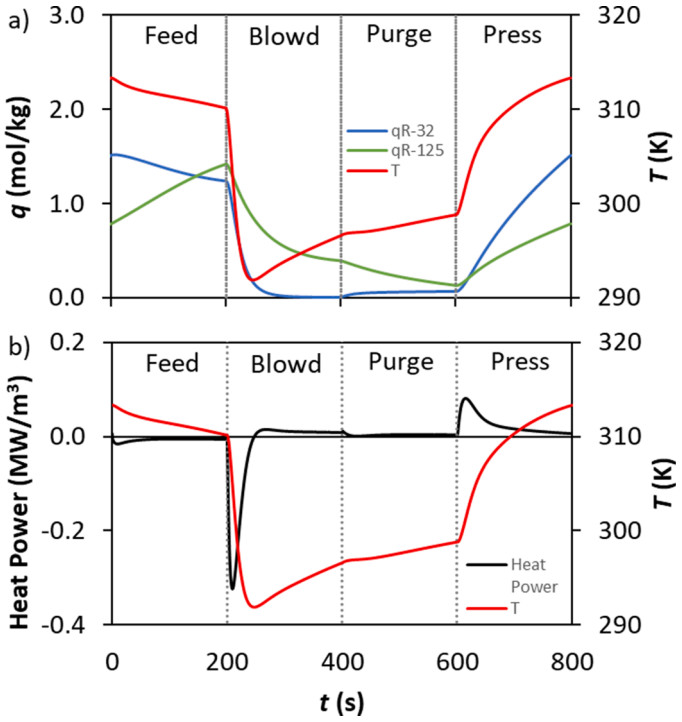

Fig. 10. Simulated history of (a) temperature (T) and adsorbed amounts of R-32 ($q_{R\text{-}32}$) and R-125 ($q_{R\text{-}125}$), and (b) the Heat Power and temperature (T) at the center of the column ($z = 0.09$ m). These results are of VSA Run 11 under CSS conditions.

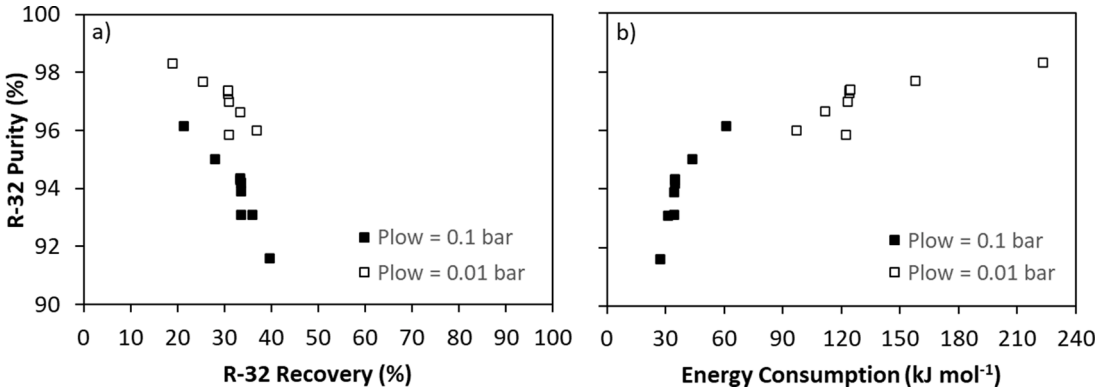

Fig. 11. R-32 purity as a function of (a) R-32 Recovery and (b) Energy consumption.

improvements in the process performance if more complex VSA cycles are developed. On the materials side, the identification and utilization of more efficient adsorbents can significantly improve the process performance. The results reported here provide a proof-of-concept of the VSA potential for the recovery of F-gases used in the refrigeration industry.

5. Conclusions

In sum, the potential of VSA processes using activated carbon for the recovery and recycling of R-32 from R-410A refrigerant blend (binary mixture of 70 mol-% R-32 and 30 mol-% R-125) was evaluated. To our knowledge, this is the first publication about the application of VSA for this separation. The main conclusions are listed below:

- A VSA cycle with four steps of equal duration (200 s each), and using a regeneration pressure of 0.1 bar, gives a R-32 purity of 93.9 mol-%, recovery of 33.6%, productivity of 4.03 mol kg^{-1} h^{-1}, and estimated energy consumption of 34.4 kJ mol^{-1}.
- An identical VSA cycle using a regeneration pressure of 0.01 bar results in R-32 purity of 96.7 mol-%, recovery of 30.9%, productivity of 4.06 mol kg^{-1} h^{-1}, and energy consumption of 123 kJ mol^{-1}. To obtain higher R-32 purities, the recovery has to be compromised.
- Process simulations show that the CSS is quickly reached after about six cycles.

Overall, the take-home message is that the results obtained demonstrate the potential of VSA processes to recover R-32 from the near-azeotropic R-410A refrigerant blend.

CRediT authorship contribution statement

Rui P.P.L. Ribeiro: Conceptualization, Methodology, Formal analysis, Investigation, Software, Visualization, Writing – original draft, Writing – review & editing. **Julio E. Sosa:** Formal analysis, Investigation, Writing – review & editing. **João M.M. Araújo:** Conceptualization, Funding acquisition, Project administration, Resources, Writing – review & editing. **Ana B. Pereiro:** Conceptualization, Funding acquisition, Project administration, Resources, Writing – review & editing. **José P.B. Mota:** Conceptualization, Methodology, Resources, Writing – review & editing.

Declaration of Competing Interest

The authors declare that they have no known competing financial interests or personal relationships that could have appeared to influence the work reported in this paper.

Acknowledgements

The authors acknowledge the financial support from the LIFE-4-Fgases project [LIFE20 CCM/ES/001748] funded by EU LIFE Programme. This work was also financed by national funds from FCT/MCTES (Portugal) through Associate Laboratory for Green Chemistry–LAQV [UIDB/50006/2020 | UIDP/50006/2020], the Norma Transitória DL 57/2016 Program Contract (R.P.P.L.R.), and the Individual Call to Scientific Employment Stimulus contracts [2020.00835.CEECIND (J.M.M.A.) / 2021.01432.CEECIND (A.B.P.)].

Supplementary materials

Supplementary material associated with this article can be found, in the online version, at doi:10.1016/j.ijrefrig.2023.01.020.

References

Ahn, H., Lee, C.H., 2003. Adsorption dynamics of water in layered bed for air-drying TSA process. Aiche J. 49, 1601–1609.
Asensio-Delgado, S., Jovell, D., Zarca, G., Urtiaga, A., Llovell, F., 2020. Thermodynamic and process modeling of the recovery of R410A compounds with ionic liquids. Int. J. Refrig. 118, 365–375.
Askalany, A.A., Saha, B.B., 2015. Experimental and theoretical study of adsorption kinetics of difluoromethane onto activated carbons. Int. J. Refrig. 49, 160–168.
Askalany, A.A., Saha, B.B., Uddin, K., Miyzaki, T., Koyama, S., Srinivasan, K., Ismail, I. M., 2013. Adsorption isotherms and heat of adsorption of difluoromethane on activated carbons. J. Chem. Eng. Data 58, 2828–2834.
Bonjour, J., Chalfen, J.B., Meunier, F., 2002. Temperature swing adsorption process with indirect cooling and heating. Ind. Eng. Chem. Res. 41, 5802–5811.
Brea, P., Delgado, J.A., Águeda, V.I., Gutiérrez, P., Uguina, M.A., 2019. Multicomponent adsorption of H2, CH4, CO and CO2 in zeolites NaX, CaX and MgX. Evaluation of performance in PSA cycles for hydrogen purification. Microporous Mesoporous Mater. 286, 187–198.
European Commission, Fluorinated greenhouse gases. Available at: https://ec.europa.eu/clima/policies/f-gas_en 2022.
Da Silva, F.A., Silva, J.A., Rodrigues, A.E., 1999. A general package for the simulation of cyclic adsorption processes. Adsorption 5, 229–244.
Esteves, I.A.A.C., Lopes, M.S.S., Nunes, P.M.C., Mota, J.P.B., 2008. Adsorption of natural gas and biogas components on activated carbon. Sep. Purif. Technol. 62, 281–296.
Fu, Q., Qin, Y., Zhang, D., Han, Y., 2018. Competitive adsorption mechanism study of CHClF2 and CHF3 in FAU zeolite. ACS Sustain. Chem. Eng. 6, 9804–9812.
Grande, C.A., Rodrigues, A.E., 2007. Layered vacuum pressure swing adsorption for biogas upgrading. Ind. Eng. Chem. Res. 46, 7844–7848.
Heath, E.A., 2017. Amendment to the Montreal protocol on substances that deplete the ozone layer (Kigali Amendment). Int. Legal Mater. 56, 193–205.
KET4F-Gas Project, http://www.ket4f-gas.eu/?page_id=1537, 2022.
Mota-Babiloni, A., Makhnatch, P., Khodabandeh, R., 2017. Recent investigations in HFCs substitution with lower GWP synthetic alternatives: focus on energetic performance and environmental impact. Int. J. Refrig. 82, 288–301.
Mota-Babiloni, A., Navarro-Esbrí, J., Barragán-Cervera, Á., Molés, F., Peris, B., 2015. Analysis based on EU Regulation No 517/2014 of new HFC/HFO mixtures as alternatives of high GWP refrigerants in refrigeration and HVAC systems. Int. J. Refrig. 52, 21–31.
Mota, J.P.B., Saatdjian, E., Tondeur, D., Rodrigues, A.E., 1995. A simulation model of a high-capacity methane adsorptive storage system. Adsorption 1, 17–27.
Motkuri, R.K., Annapureddy, H.V.R., Vijaykumar, M., Schaef, H.T., Martin, P.F., McGrail, B.P., Dang, L.X., Krishna, R., Thallapally, P.K., 2014. Fluorocarbon adsorption in hierarchical porous frameworks. Nat. Commun. 5, 4368.

Pardo, F., Zarca, G., Urtiaga, A., 2021. Effect of feed pressure and long-term separation performance of Pebax-ionic liquid membranes for the recovery of difluoromethane (R32) from refrigerant mixture R410A. J. Membr. Sci. 618, 118744.
Ribeiro, R.P.P.L., Esteves, I.A.A.C., Mota, J.P.B., 2017. Two-column relay simulated moving-bed process for gas-phase separations. Sep. Purif.Technol. 182, 19–28.
Ribeiro, R.P.P.L., Grande, C.A., Rodrigues, A.E., 2011. Adsorption of water vapor on carbon molecular sieve: thermal and electrothermal regeneration study. Ind. Eng. Chem. Res. 50, 2144–2156.
Savitz, S., Siperstein, F.R., Huber, R., Tieri, S.M., Gorte, R.J., Myers, A.L., Grey, C.P., Corbin, D.R., 1999. Adsorption of hydrofluorocarbons HFC-134 and HFC-134A on X and Y zeolites: effect of ion-exchange on selectivity and heat of adsorption. J. Phys. Chem. B 103, 8283–8289.
Shiflett, M.B., Corbin, D.R., Elliott, B.A., Yokozeki, A., 2013a. Sorption of trifluoromethane in zeolites and ionic liquid. J. Chem. Thermodyn. 64, 40–49.
Shiflett, M.B., Corbin, D.R., Yokozeki, A., 2013b. Comparison of the sorption of trifluoromethane (R-23) on zeolites and in an ionic liquid. Adsorpt. Sci. Technol. 31, 59–83.
Sircar, S., Golden, T.C., 2000. Purification of hydrogen by pressure swing adsorption. Sep. Sci. Technol. 35, 667–687.
Sircar, S., Kratz, W.C., 1989. Oxygen production by pressure swing adsorption. Sep. Sci. Technol. 24, 429–440.
Sosa, J.E., Malheiro, C., Castro, P.J., Ribeiro, R.P.P.L., Piñeiro, M.M., Plantier, F., Mota, J.P.B., Araújo, J.M.M., Pereiro, A.B., 2023. Exploring the potential of metal–organic frameworks for the separation of blends of fluorinated gases with high global warming potential. Global Challenges 7, 2200107.
Sosa, J.E., Malheiro, C., Ribeiro, R.P.P.L., Castro, P.J., Piñeiro, M.M., Araújo, J.M.M., Plantier, F., Mota, J.P.B., Pereiro, A.B., 2020a. Adsorption of fluorinated greenhouse gases on activated carbons: evaluation of their potential for gas separation. J. Chem. Technol. Biotechnol. 95, 1892–1905.
Sosa, J.E., Santiago, R., Hospital-Benito, D., Costa Gomes, M., Araújo, J.M.M., Pereiro, A. B., Palomar, J., 2020b. Process evaluation of fluorinated ionic liquids as F-gas absorbents. Environ. Sci. Technol. 54, 12784–12794.
United States Environmental Protection Agency: Overview of Greenhouse Gases. Available at: https://www.epa.gov/ghgemissions/overview-greenhouse-gases, 2022.
Wanigarathna, D.J.A., Gao, J., Takanami, T., Zhang, Q., Liu, B., 2016. Adsorption separation of R-22, R-32 and R-125 fluorocarbons using 4A molecular sieve zeolite. ChemistrySelect 1, 3718–3722.
Wanigarathna, D.K.J.A., Gao, J., Liu, B., 2018a. Fluorocarbon separation in a thermally robust zirconium carboxylate metal–organic framework. Chem. – Asian J. 13, 977–981.
Wanigarathna, D.K.J.A., Liu, B., Gao, J., 2018b. Adsorption separation of R134a, R125, and R143a fluorocarbon mixtures using 13X and surface modified 5A zeolites. AIChE J. 64, 640–648.
Yamauchi, H., Kodama, A., Hirose, T., Okano, H., Yamada, K.I., 2007. Performance of VOC abatement by thermal swing honeycomb rotor adsorbers. Ind. Eng. Chem. Res. 46, 4316–4322.
Yancey, A.D., Corbin, D.R., Shiflett, M.B., 2022a. Difluoromethane (HFC-32) and pentafluoroethane (HFC-125) sorption on linde type A (LTA) zeolites for the separation of azeotropic hydrofluorocarbon refrigerant mixtures. Langmuir 38, 1937–1953.
Yancey, A.D., Terian, S.J., Shaw, B.J., Bish, T.M., Corbin, D.R., Shiflett, M.B., 2022b. A review of fluorocarbon sorption on porous materials. Microporous Mesoporous Mater. 331, 111654.
Zheng, J., Vemuri, R.S., Estevez, L., Koech, P.K., Varga, T., Camaioni, D.M., Blake, T.A., McGrail, B.P., Motkuri, R.K., 2017. Pore-engineered metal–organic frameworks with excellent adsorption of water and fluorocarbon refrigerant for cooling applications. J. Am. Chem. Soc. 139, 10601–10604.